# Earth Abundant Perovskite Oxides for Low Temperature CO<sub>2</sub> Conversion

Debtanu Maiti, Bryan J. Hare, Yolanda A. Daza, Adela E. Ramos, John N. Kuhn\*, Venkat R. Bhethanabotla\*

Department of Chemical & Biomolecular Engineering, University of South Florida, Tampa, FL 33620.

\*Correspondence to: <u>bhethana@usf.edu</u>; <u>jnkuhn@usf.edu</u>

#### **Abstract:**

Conversion of CO<sub>2</sub> in a scalable technology has a potential for enormous energy and environmental impact but remains a challenge. We present several stable, earth abundant perovskite oxide materials for reverse water gas shift chemical looping (RWGS-CL) process as a potential solution for this CO<sub>2</sub> mitigation problem. These materials and process combination circumvents issues plaguing other emerging technologies, viz. poor rates of CO<sub>2</sub> conversion, high operation temperatures, use of precious metal catalysts, or combinations thereof. Using DFT-calculated oxygen vacancy formation energy, a key descriptor for RWGS-CL process, we have successfully predicted several earth abundant perovskite oxides with high CO<sub>2</sub> conversion capability. We simultaneously achieved 100% selective CO generation from CO<sub>2</sub> at highest known rates (~160 µmoles/min/gram perovskite oxide) at record low process temperatures of 450-500 °C using lanthanum and calcium based perovskite oxides. These materials are stable over several RWGS-CL cycles, enabling industrial implementation.

### **Broader Context**

The adverse effects of global warming and climate change have led to a shift of focus from efficient fossil fuel generation to sustainable generation of renewable energy. However, even with a paradigm shift from fossil fuel based energy to electricity based energy economy, certain sectors like heavy transportation would still require hydrocarbon fuels. This particular energy dependence demands a sustainable carbon-neutral fuel production scheme posing no threats on the environment. Meanwhile, atmospheric carbon dioxide mitigation is a major goal being targeted globally. Repurposing this carbon dioxide to high value carbon-based products like fuels presents a novel approach. Several methodologies have been reported for this purpose of hydrocarbon generation from carbon dioxide. However, most of them are limited by certain factors that restricts their implementation in large scale. This article reports a process that can potentially be implemented industrially. The materials developed for this purpose are earth abundant, stable, and capable of serving for sustainable low temperature CO<sub>2</sub> conversion platforms.

### 1. Introduction

Increasing atmospheric  $CO_2$  is the primary cause for climate change and associated global environmental problems. Carbon capture and storage (CCS) is recognized as a solution to this  $CO_2$  problem and is attracting considerable investment. However, the annual scale of  $CO_2$  capture (35 Mt as of early 2017)<sup>2</sup> is far below the global  $CO_2$  emissions from fossil fuel use (~35

Gt in 2015).<sup>3</sup> Repurposing CO<sub>2</sub> for renewable energy generation presents an exciting alternative<sup>4,</sup> <sup>5</sup> and a number of different routes have been proposed and investigated. <sup>6-8</sup> Two notable ones are photocatalytic splitting of CO<sub>2</sub><sup>9</sup> and solar thermochemical conversion of CO<sub>2</sub> to CO<sup>10-12</sup>, which suffer from poor rates and high operating temperatures, respectively. Here, we present a method to address these limitations using materials and a process, which serve as a perfect platform for sustainable CO<sub>2</sub> conversion. Photocatalysis is a low temperature process but struggles with extremely low CO<sub>2</sub> conversion rates, making it unsuitable for industrial application. Solar thermochemical splitting can achieve superior rates, but at the cost of high operation temperatures (more than 1000 °C, see Supplementary Fig. 1 and Table S1)<sup>10, 13-22</sup> and a limited array of stable materials. The solar thermochemical approach has attracted recent attention in particular as the sun-to-fuel (STF) efficiency is the highest amongst several other methodologies.<sup>23</sup> In solar thermochemical conversion, metal oxides like ceria and mixed metal oxides like perovskite oxides are suitable for converting CO<sub>2</sub> to CO. <sup>10, 24</sup> Our process for solar thermochemical splitting, reverse water gas shift- chemical looping (RWGS-CL) (Fig 1.), operates at much lower temperatures of about 500-600 °C with even higher CO<sub>2</sub> conversion rates. 14, 15, 25 The goal of converting CO<sub>2</sub> to hydrocarbons can be attained once we have sustainable conversion of CO<sub>2</sub> to CO via RWGS-CL, by subsequent hydrogenation of CO to fuels via Fischer Tropsch Synthesis (FTS). Thus, lowering the operating temperature of RWGS-CL to that of FTS is one of the biggest challenges today.

RWGS-CL is essentially a two-step process in which an oxide material (like a unary metal oxide or perovskite oxide, ABO<sub>3</sub>) is first reduced under hydrogen flow to form oxygen deficient structures (ABO<sub>3-δ</sub>). These oxygen vacancies act as active sites for CO<sub>2</sub> conversion. In the second step, CO<sub>2</sub> flows over these materials and converts to CO, while the oxygen vacant materials regain their full stoichiometry (ABO<sub>3</sub>). High oxygen mobility of the perovskite oxides allows for operation of these looping cycles without phase change of the oxides. The process is depicted in Fig. 1. This allows for generation of CO, a precursor for hydrocarbon production via FTS, in a sustainable process. Using renewable hydrogen for the entire process, the (STF) efficiency is highly improved<sup>26</sup> with high rates of CO<sub>2</sub> conversion at FTS compatible temperatures. We anticipate this methodology of CO<sub>2</sub> repurposing towards hydrocarbon generation can significantly impact the current energy market. Perovskite oxides are the main vehicles for conversion of CO<sub>2</sub> to CO using RWGS-CL. These mixed metal oxides are predominant in cubic, hexagonal and orthorhombic phases, with cubic phases being the most stable at high temperatures. <sup>27-29</sup> Usually, these ABO<sub>3</sub> structures are composed of lanthanides or alkaline earth metals on the 'A' sites and transition metals on the 'B' sites. Lanthanum based materials have shown great promise in solar thermochemical cycles (STC).<sup>30,31</sup> The cubic forms of these structures comprise of hexa-coordinated 'B' site elements and dodeca-coordinated 'A' site elements. The different surface facets can have varying concentrations of 'A' and 'B' site elements. Stability of their (100) and (110) planes has also been reported.<sup>32</sup> The mechanism of RWGS-CL is primarily dependent on the creation of oxygen vacancies on these surfaces and CO<sub>2</sub> conversion on those oxygen vacant sites. This phenomenon varies with different neighboring elements and their lattice structure, implying that material structure and composition of these ABO<sub>3</sub> type perovskite oxides play a significant role in tuning the oxygen vacancy characteristics of these materials. Probing these oxygen vacant sites on varying perovskite oxide compositions is thus imperative for better formulation of catalysts and understanding their role in carbon dioxide conversion. Density functional theory (DFT) based oxygen vacancy formation energy calculations can provide the perfect insights of these materials. Using oxygen vacancy

formation energy as an appropriate descriptor for this RWGS-CL process, we henceforth predicted several earth abundant perovskite oxides with potential toward sustainable carbon dioxide conversion. Experiments conducted over these predicted materials demonstrated superior carbon dioxide conversion performance at sustainable temperatures. These materials along with the improved CO<sub>2</sub> conversion capabilities are promising for feasible industrial implementation.

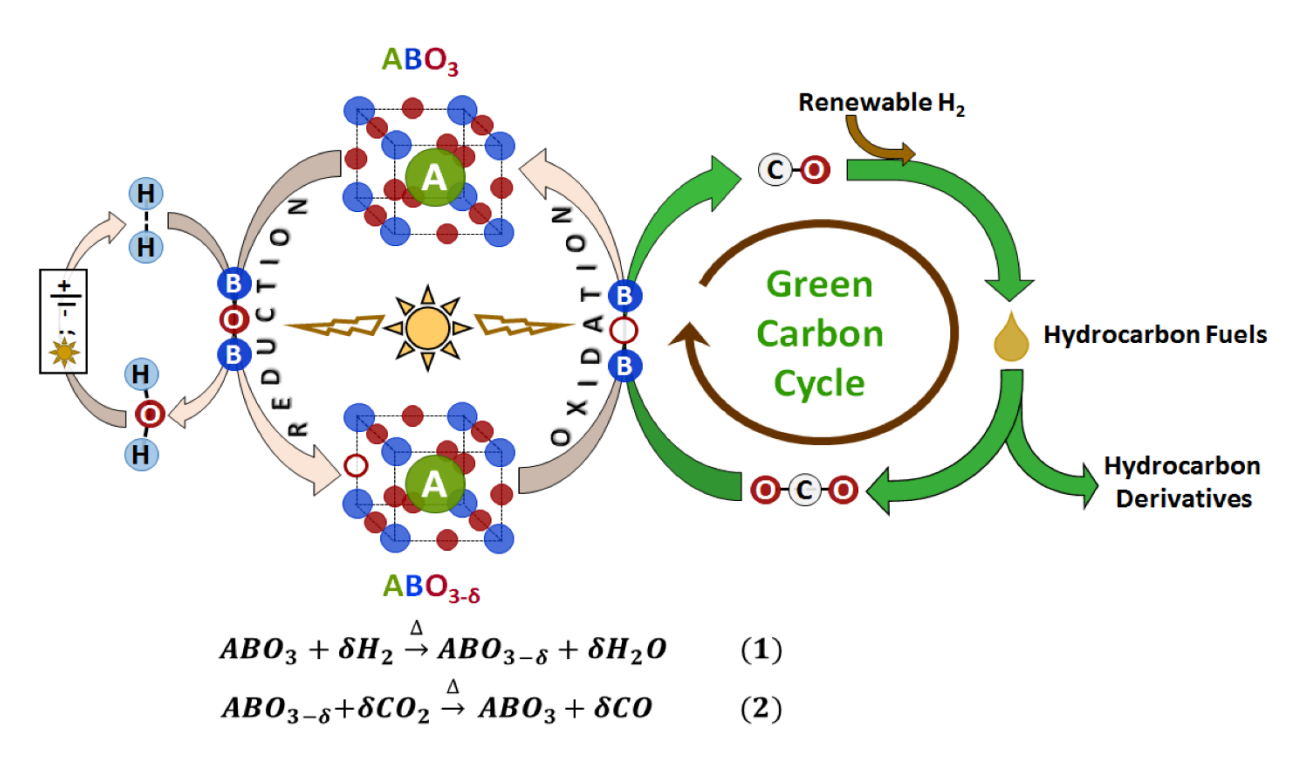


Figure 1 | Schematic diagram of the RWGS-CL process demonstrating the two-step conversion of CO<sub>2</sub> to CO, a feedstock for hydrocarbon generation, via ABO<sub>3</sub> type perovskite oxides. Equation 1 and 2 depict the perovskite reduction and oxidation reaction, respectively.

### **Materials and Methods**

### Computational Methods

Density functional theory (DFT) based calculations were performed using Vienna ab initio Simulation Package (VASP -5.3.3). <sup>33-37</sup> All the calculations used the plane wave basis set and gradient generalization for the approximation of electron densities. The core electronic states were treated by projector augmented wave (PAW) potentials <sup>38</sup> and Perdew-Burke-Ernzerhof (PBE)<sup>39</sup> variant of exchange correlation. Consistent use of default potentials for all the elements was maintained. Throughout the study, a constant energy cut off of 600 eV was used. The convergence criterion for the ionic relaxations is set at 0.001 eV/atom. All the bulk phase systems studied were cubic, with 40 atoms in a  $2 \times 2 \times 2$  supercell, while the surface slabs were made of

2×2×2 supercells having 40 atoms with 15 Å of vacuum along the surface direction to mimic the absence of atomic periodicity on surfaces. After convergence with respect to k point sampling was checked, calculations for all the 40 atom supercell of bulk stoichiometric and non-stoichiometric perovskites were done with 4×4×4 k point mesh generated by an automatic scheme having Monkhorst Pack grid. Magnetic effects were not considered explicitly as they are known to have minor effects in the systematic trends of energy. For the slab calculations of the surface structures, dipole correction was accounted.

The initial ground state configurations for each of the materials were obtained through a series of varying cell volume calculations. Once the ground state lattice constant was established, the entire set of parameters were used for the nonstoichiometric calculations as well. Though oxygen vacancy formation in a material is a complex process consisting of several steps, the major energy intensive step is the dissociation of the metal-oxygen bond. Hence, computational oxygen vacancy formation energies calculated as enthalpy difference between the initial stoichiometric material and the final oxygen deficient material along with gas phase oxygen mostly represents the energy barrier for the dissociation of the metal-oxygen bonds and the subsequent relaxation of the oxygen deficient structure. The creation of oxygen vacancies is marked by systematic removal of oxygen atoms, either from bulk or surface. The extent of oxygen vacancy ( $\delta$ ) was defined as oxygen deficiency per unit molecule of ABO<sub>3</sub>; thus in a 40 atom supercell of perovskites,  $\delta = 0.125$  is marked by removal of one oxygen atom. For surface oxygen vacancies of  $\delta = 0.125$ , the number of oxygen atoms removed from the 40 atom supercell is one as well. The oxygen vacancy formation energy is calculated as

$$E_{vac} = E_{ABO_{(3-\delta)}} + \delta \times \frac{n}{2} E_{O_2} - E_{ABO_3} \dots [1]$$

where,  $E_{ABO_3}$  is the total energy of the pure stoichiometric perovskite supercell of n unit cells, while  $E_{ABO_{(3-\delta)}}$  is that of the oxygen vacant perovskite supercell, 'n' representing the number of unit cells considered (8 for both bulk and surface calculations) and  $E_{O_2}$  is the molecular energy of oxygen. The oxygen over-binding error has been addressed by Wang et al.<sup>42</sup> for PBE functionals by using a correction factor of 1.36 eV. All the calculations of oxygen vacancy formation energy were corrected by this factor. The oxygen adsorption energy on the materials is calculated using

$$E_{ads} = E_{P+O_2} - E_{O_2} - E_P \dots [2]$$

where,  $E_P$  is the energy of either pure or oxygen vacant perovskite,  $E_{P+CO_2}$  is the energy of combined system of  $O_2$  adsorbed on the perovskite while  $E_{O_2}$  is the energy of molecular gaseous oxygen.

The empirical modelling for the bulk oxygen vacancy formation energy has been done with respect to two intrinsic parameters for the materials that closely govern oxygen vacancy formation. Enthalpy of formation is a measure of stability of a material. It has been calculated based on the difference of the pure phase enthalpy of a material and the enthalpy of its pure phase elemental components. Bond dissociation energy is closely related to vacancy formation energy. The bond dissociation energy is approximately calculated as per the total energy to break two 'B-O' bonds and four 'A-O' bonds (based on two 'B' sites and four 'A' sites as the closest neighbors of an oxygen atom) in a perovskite cubic structure. The data from the handbook of

chemical bond energies<sup>43</sup> were used for the purpose of estimating the bond dissociation energy associated with an oxygen vacancy formation.

## **Experimental Methods**

Perovskite samples of the form,  $A1_{(1-x)}A2_xB1_{(1-y)}B2_yO_3$ , were synthesized by the Pechini method.<sup>44</sup> Metal nitrates and carbonates, as obtained from Alfa-Aesar or Sigma Aldrich, were used as precursors. They were dissolved in a citric acid solution (a chelating agent) by stirring for 2 hr at 60 °C. Ethylene glycol (Aldrich > 99%) was subsequently added followed by stirring for 7 hr at 90 °C. The resultant gel was then charred at 450 °C (25 °C/min) for 2 hr and then crushed to a fine powder. A final calcination step was thereby conducted over this powder at 950 °C to obtain fresh samples of stoichiometric perovskite oxides.

Crystalline structures were analyzed using X-Ray Diffraction (XRD) in a Bruker X-ray diffractometer with a Cu K $\alpha$  source. The resulting diffraction patterns collected from 20 to 100 (20°) with a step size of 0.0102 20° confirmed the presence of a dominant perovskite oxide phase in each sample. XRD was conducted on both pure phase samples and at post-reaction conditions to determine the stability of these materials. X-ray photoelectron spectrometry (XPS) measurements were conducted with a Thermo Scientific K-Alpha instrument using Al K $\alpha$  radiation. The C1s peak was located at 284.85 eV. Transmission emission microscopy (TEM) was conducted on these samples using a Tecnai F20 TEM, with a Schottky field emitter as the electron source with a minimal energy spread of less than 0.7 eV and a line resolution of 0.24 nm. Hitachi S-800 scanning electron microscope with EDAX-Phoenix EDS system was used to probe the samples.

The  $CO_2$  conversion experiments via RWGS-CL were conducted in a quartz U-tube reactor. The samples were packed between glass wool in the reactor and placed in a Thermo-Scientific tube furnace. All temperature-programmed experiments were conducted in this setup with changes in gas flow (as controlled by Alicat mass flow controllers) and temperatures (heating rate being kept constant at  $10\,^{\circ}$ C/min). UHP grade gases, as obtained from Airgas, were used for these reactions. Oxygen vacancy formation under hydrogen (10% H<sub>2</sub>/He) was measured by temperature-programmed reduction (TPR) from ambient temperature to 950 °C. Temperature-programmed oxidation (TPO) experiments were conducted to detect the conversion of  $CO_2$  to CO. A MKS Cirrus mass spectrometer was used to monitor the reactor effluent (m/z = 18 signal for the detection of water, representing oxygen vacancy formation, and m/z = 28 signal for the detection of CO, representing  $CO_2$  conversion). An isothermal reduction for 30 min at 550 °C was then ensued under hydrogen with helium as carrier (10% H<sub>2</sub>/He). These reduced samples were cooled naturally under He flow and subsequently heated back to 950 °C under  $CO_2$  flow (10%  $CO_2$ /He) for generation of CO. The RWGS-CL cycle experiments were all conducted at 550 °C with 20 min for each of reduction and oxidation steps.

### **Results and Discussions**

Perovskite oxides have shown promising response towards  $CO_2$  conversion to CO via RWGS-CL process and density functional theory (DFT) based oxygen vacancy formation energy ( $E_{vac}$ ) provides the insights into a material's oxygen vacancy formation abilities. We have recently shown that these DFT calculated  $E_{vac}$  clearly corresponds to the extent of oxygen

vacancy formation and temperature of vacancy formation in the RWGS-CL process.<sup>32</sup> Deml et al. have shown the correspondence of E<sub>vac</sub> to STC experiments. <sup>30, 31, 45</sup> Thus, it is reasonable to expect that E<sub>vac</sub> is an accurate descriptor for the RWGS-CL process. Therefore, we use this descriptor for the prediction of perovskite oxides with CO<sub>2</sub> conversion capabilities in RWGS-CL process. From our previous work, La<sub>0.75</sub>Sr<sub>0.25</sub>FeO<sub>3</sub> (LSF) exhibited the best CO<sub>2</sub> conversion results, whereby isothermal RWGS-CL cycles were conducted at 550 °C. 15 Since perovskite oxides are perfect platforms for material composition tuning, we screened materials having different elemental compositions in both the 'A' and 'B' sites. For simplicity, the different perovskite oxide compositions were classified into four major groups: ABO<sub>3</sub> (only a single element 'A' and another element 'B' ), A1<sub>0.5</sub>A2<sub>0.5</sub>BO<sub>3</sub> (two elements A1 and A2 in equal compositions at the 'A' site, with only one element in the 'B' site), AB1<sub>0.5</sub>B2<sub>0.5</sub>O<sub>3</sub> (two elements B1 and B2 in equal compositions in the 'B' site), and A1<sub>0.5</sub>A2<sub>0.5</sub>B1<sub>0.5</sub>B2<sub>0.5</sub>O<sub>3</sub> (two elements A1 and A2 in the 'A' site and two elements B1 and B2 in the 'B' site). For the 'A' site, we chose lanthanum, calcium, strontium and barium while for 'B' site we selected the 3d elements from chromium to copper (Cr, Mn, Fe, Co, Ni and Cu) along with aluminum and gallium on the basis of several previous reports of successful thermochemical (TC) and RWGS-CL processes. 14, 15, 46, <sup>47</sup> The representative crystal structures of these perovskite oxides are shown in Supplementary Fig. 2. We calculated the enthalpy of formation of these materials to test their stability and subsequently their E<sub>vac</sub> to predict their performance in RWGS-CL.

The search for the best-performing perovskite oxides with CO<sub>2</sub> conversion capabilities is done based on their oxygen vacancy formation energies. In a typical RWGS-CL experiment, the extent of oxygen vacancies ( $\delta$ ) formed in a perovskite oxide, ensuring the stability of the perovskites, is about 0.1 - 0.4.<sup>15</sup> It has also been shown that the trends of oxygen vacancy formation energy across different materials remain the same for different extents of oxygen vacancy ( $\delta = 0.125, 0.25, 0.375$ ). Thus, for screening purposes, we only calculated the energy required to create  $\delta$ =0.125 extent of oxygen vacancy. Since LSF presented the current best case scenario for RWGS-CL, <sup>15, 16, 32, 48, 49</sup> we calculated the E<sub>vac</sub> for LSF and used this E<sub>vac</sub> as reference. The site-averaged oxygen vacancy formation energy in a LSF crystal was found to be 3.36 eV. Based on this E<sub>vac</sub> value, we have screened the perovskite oxides. Any material having similar oxygen vacancy formation energy is expected to exhibit similar oxygen vacancy formation in the RWGS-CL process. A material with higher E<sub>vac</sub> is more reluctant to lose oxygen and may either create fewer oxygen vacancies at a certain temperature, or will require a higher temperature to create the same number of oxygen vacancies. Similarly, a material having lower E<sub>vac</sub> is more prone to accommodate oxygen vacancies and will be reduced easily during the RWGS-CL process with hesitation to re-oxidize. In this work, we focused only on materials having  $E_{vac}$  of  $(3.36 \pm 0.5)$  eV. As seen in Fig. 2A,  $E_{vac}$  is plotted for different ABO<sub>3</sub>. As reported in literature, there is a consistent decreasing trend of E<sub>vac</sub> with transition elements.<sup>41</sup> In a very similar way, the oxygen vacancy formation energies of all the different perovskite oxide species (A1<sub>0.5</sub>A2<sub>0.5</sub>BO<sub>3</sub>, AB1<sub>0.5</sub>B2<sub>0.5</sub>O<sub>3</sub>, and A1<sub>0.5</sub>A2<sub>0.5</sub>B1<sub>0.5</sub>B2<sub>0.5</sub>O<sub>3</sub>) have been plotted in Fig. 2B, 2C and 2D, respectively. We found several materials that lie in our preferred energy zone of  $(3.36 \pm$ 0.5), as marked by the red dotted box in Fig. 2 (A-D). All of these calculations are based on the minimum energy configurations of these perovskite oxides. As shown in Table S1, there exist minor E<sub>vac</sub> variations for different configurations. However, we expect this to have minor effect on our prediction model as we have performed the calculations on a consistent basis of minimum-energy configuration (i.e., the trends of E<sub>vac</sub> should not change) and also the E<sub>vac</sub>

variation (1eV) in proposed our optimum range is larger than configuration-dependent energy variation (less than 0.2 eV).

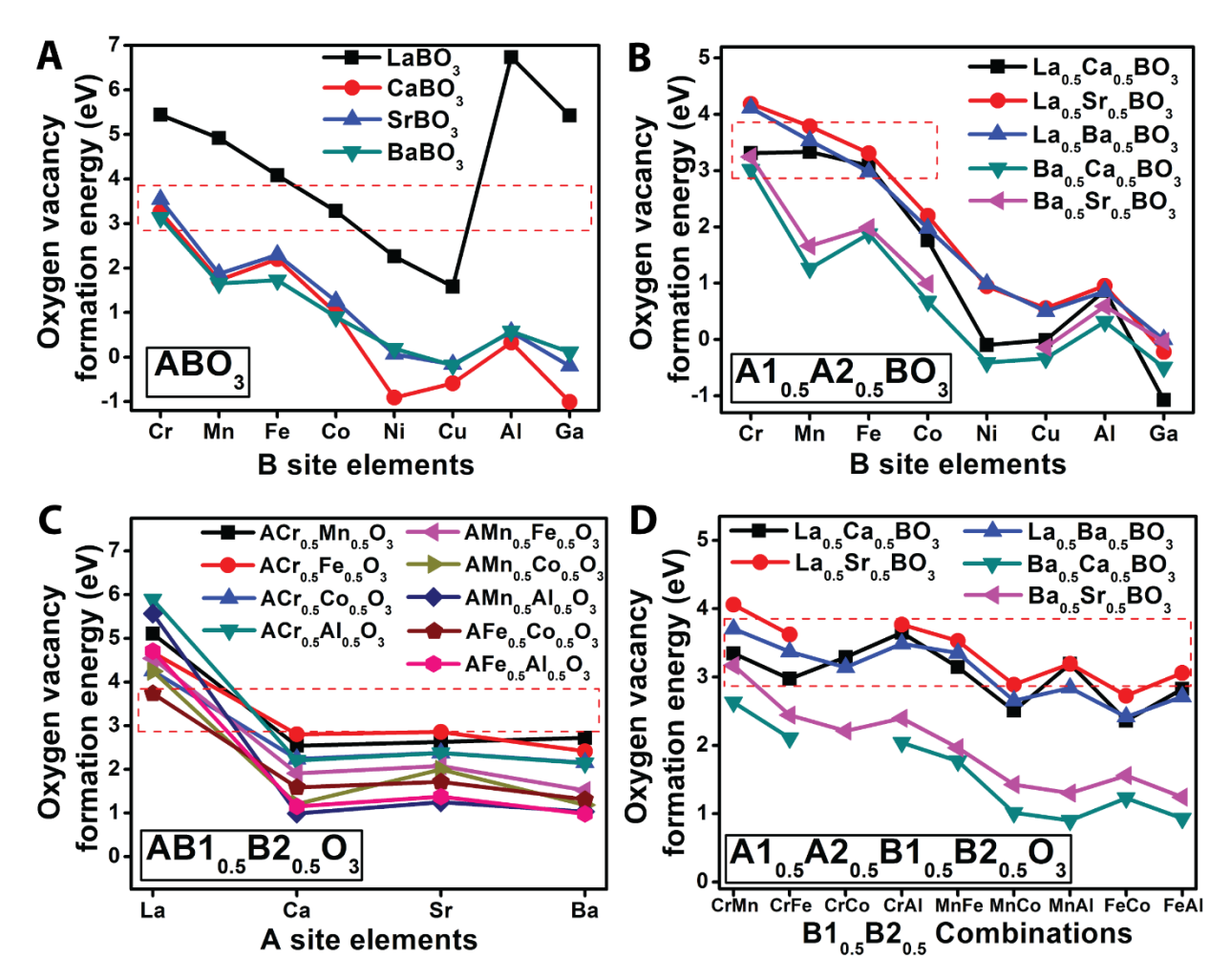
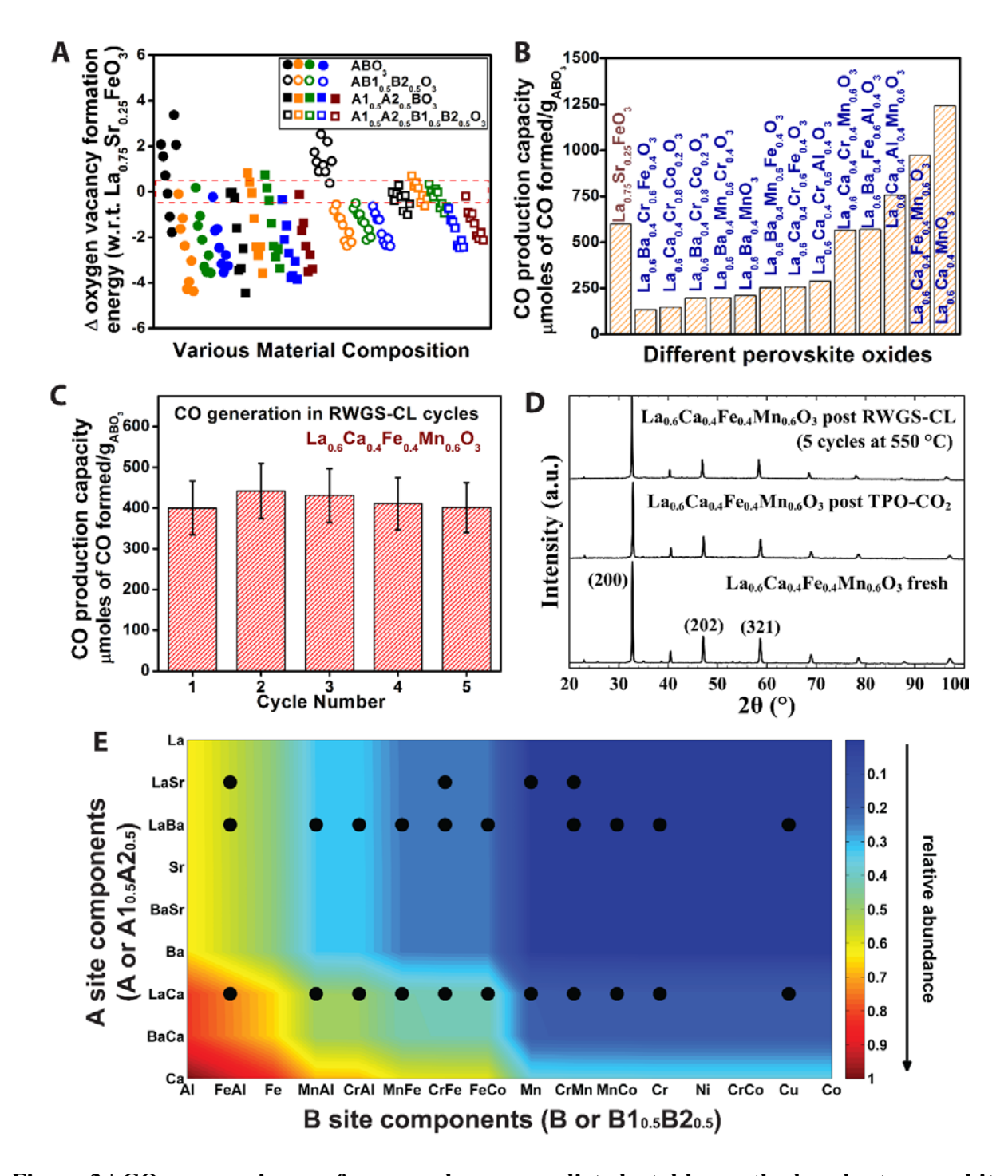


Figure 2 | Oxygen vacancy formation energies ( $E_{vac}$ ) for different perovskite oxides. A,  $E_{vac}$  required to create an oxygen vacancy extent of  $\delta = 0.125$  in ABO<sub>3</sub> type perovskite oxides where 'A' sites are La, Ca, Sr or Ba while 'B' sites are the 3d elements Cr - Cu along with Al and Ga. B,  $E_{vac}$  required to create an oxygen vacancy extent of  $\delta = 0.125$  in A1<sub>0.5</sub>A2<sub>0.5</sub>BO<sub>3</sub> type of perovskite oxides with mixtures of Al and A2 elements forming the 'A' site. C,  $E_{vac}$  required to create an oxygen vacancy extent of  $\delta = 0.125$  in AB1<sub>0.5</sub>B2<sub>0.5</sub>O<sub>3</sub> type of perovskite oxides with mixtures of B1 and B2 elements forming the 'B' site. D,  $E_{vac}$  required to create an oxygen vacancy extent of  $\delta = 0.125$  in A1<sub>0.5</sub>A2<sub>0.5</sub>B1<sub>0.5</sub>B2<sub>0.5</sub>O<sub>3</sub> type of perovskite oxides. The red dotted box in all the figures (a-d) presents the materials showing favorable oxygen vacancy formation energies.

The cumulative oxygen vacancy formation characteristic for these perovskite oxides is plotted in Fig. 3A. Here, we compare each material's oxygen vacancy formation energy to that of LSF and hence, materials exhibiting minimal deviation from LSF's E<sub>vac</sub> value are anticipated to behave similarly to LSF. The red dotted box in Fig. 3A shows the potential candidates for CO<sub>2</sub>

conversion. Several of these materials were synthesized via Pechini method (XRD patterns shown in Fig. S3)<sup>44</sup> and subsequently tested for CO<sub>2</sub> conversion capabilities in temperatureprogrammed experiments. Fig. 3B presents the CO formation yields using these perovskite oxides. Lanthanum and calcium based materials show remarkable performance. La<sub>0.6</sub>Ca<sub>0.4</sub>MnO<sub>3</sub> is capable of producing twice the amount of CO (1242 µmoles/gram perovskite oxide) than that from LSF (599 µmoles/gram perovskite oxide) with CO production rates almost 1.85 times higher than that of LSF (60.5 µmoles/min/gram of LSF). La<sub>0.6</sub>Ca<sub>0.4</sub>Fe<sub>0.4</sub>Mn<sub>0.6</sub>O<sub>3</sub> shows unprecedented CO production rates of about 160 µmoles/min/gram perovskite oxide with total CO yield of 973 umoles/gram perovskite oxide. The detailed information of CO<sub>2</sub> conversion by these perovskite oxides is reported in Table S2. The percentage CO<sub>2</sub> conversion as reported in Table S2 is quite low and does not truly reflect the potential of the process. Further process optimization in terms of shorter reaction-times (in the form of quick pulses of reduction/oxidation cycles), and reduction of CO<sub>2</sub> feed volume will definitely enhance this CO<sub>2</sub> conversion extent. Since CO<sub>2</sub> conversion is largely dependent on the material composition, minor composition tuning of these materials could result in even better CO<sub>2</sub> conversion results, which will allow for potential implementation of this RWGS-CL process at large scale. The long-term stability of these materials and their applicability were tested as well. Fig. 3C shows consistent generation of CO by La<sub>0.6</sub>Ca<sub>0.4</sub>Fe<sub>0.4</sub>Mn<sub>0.6</sub>O<sub>3</sub> over repeated cycles at 550 °C while Fig. 3D explicitly shows the stability of La<sub>0.6</sub>Ca<sub>0.4</sub>Fe<sub>0.4</sub>Mn<sub>0.6</sub>O<sub>3</sub> structure throughout these RWGS-CL cycles. The long-term applicability of these perovskite materials is related to their abundance. The relative earth abundance plot of the 'A' and 'B' site composition of these perovskite oxides (Fig. 3E) shows easy availability of several of our predicted materials. <sup>50</sup> La<sub>0.6</sub>Ca<sub>0.4</sub>Fe<sub>0.4</sub>Mn<sub>0.6</sub>O<sub>3</sub> as can be seen in Figure 3E, presents an earth abundant option with low material and processing costs. This particular perovskite oxide not only demonstrates a stable and consistent high CO<sub>2</sub> conversion performance at low temperatures, but is also a sustainable candidate for industrial use.



**Figure 3** | **CO<sub>2</sub>** conversion performance by our predicted, stable, earth abundant perovskite oxides. **A,** Difference of E<sub>vac</sub> for all the perovskite oxides with respect to that of LSF, the red dotted box showing the materials with possible CO<sub>2</sub> conversion capabilities. **B,** Experimental CO yields of the predicted perovskite oxides, lanthanum and calcium based ones showing improved CO<sub>2</sub> conversion performance than LSF. **C,** CO<sub>2</sub> conversion performance by La<sub>0.6</sub>Ca<sub>0.4</sub>Fe<sub>0.4</sub>Mn<sub>0.6</sub>O<sub>3</sub> perovskite oxide in RWGS-CL cycles at 550 °C. **D,** Structural stability of La<sub>0.6</sub>Ca<sub>0.4</sub>Fe<sub>0.4</sub>Mn<sub>0.6</sub>O<sub>3</sub> after TPO-CO<sub>2</sub> and 5 RWGS-CL cycles, showing the potential for using

these materials over several cycles. **E**, A relative earth abundance plot of the 'A' site and 'B' site compositions of these materials.

These materials call for more research towards high-value chemical formation from CO<sub>2</sub>. A lot of research effort, in recent times, is focused on catalytic hydrogenation of CO<sub>2</sub> to hydrocarbons. <sup>20, 49, 51-54</sup> However, these approaches suffer from some key issues like conversion extent, selectivity, energy efficiency etc. Per Kondratenko et al., CO<sub>2</sub> hydrogenation to fuels is a need of the society and can provide much better performance than photochemical or electrochemical routes, which suffer from low rates and low Faradaic efficiencies, respectively.<sup>20</sup> However, key issues with current H<sub>2</sub> sources are coking and sulfur poisoning of the steam reforming catalysts. This has led to the choice of water being the best source for renewable hydrogen. One of the better performing materials for 100% selective methane formation from CO<sub>2</sub> reported a rate of 40 nmol of CH<sub>4</sub> per min per gcat.<sup>55</sup> Moreover, it was also emphasized that CO is a key intermediate of CO<sub>2</sub> to hydrocarbon route and enhancing CO<sub>2</sub> to CO reactivity is a great way towards feasible hydrocarbon generation from CO<sub>2</sub>. <sup>56</sup> Our process makes a significant contribution towards a sustainable solution for CO<sub>2</sub> to fuels. It demonstrates 100% selective CO generation at low temperatures of ~450 °C. The rates of CO generation are several orders higher than most photocatalytic processes.<sup>20</sup> Plasma based routes are also studied in recent times, however more effort is needed towards optimizing energy efficiency, syngas production rates and CO<sub>2</sub> conversion rates.<sup>54</sup> The importance of these CO<sub>2</sub> to hydrocarbon routes is also evident from studies focused on understanding the reaction mechanisms over various catalytic systems.<sup>52</sup> The current limitation of the existing technologies is depicted in terms of poor rates of methanol selectivity and methanol production rates (0.40 – 10.9 mol/kg-cat/hr). Expenses Reidel et al. also stated the importance of CO formation and its role as a key intermediate for hydrogenation reaction. This perspective calls for active research and improvement of CO generation from CO<sub>2</sub>, which can be subsequently converted to hydrocarbons. The perovskite oxides reported here demonstrate superior CO<sub>2</sub> conversion performance that allows for hydrocarbon generation at large scale.

The better performing materials were further investigated via transmission electron microscopy (TEM), scanning electron microscopy (SEM), energy-dispersive x-ray spectroscopy (EDS) and x-ray photoelectron spectroscopy (XPS). Figures 4 (A-C) reveal the TEM micrographs of La<sub>0.75</sub>Sr<sub>0.25</sub>FeO<sub>3</sub>, La<sub>0.6</sub>Ca<sub>0.4</sub>MnO<sub>3</sub> and La<sub>0.6</sub>Ca<sub>0.4</sub>Fe<sub>0.4</sub>Mn<sub>0.6</sub>O<sub>3</sub> samples at prereaction conditions. The samples show nanoparticle formation in approximately 100-250 nm size range. Fine nanospheres are also found in LSF samples (Fig. 4A-inset). HRTEM images reveal the *d*-spacing of the representative peaks of the perovskite crystals. No other crystalline phase was detected, in accord with XRD results. Presence of constituent elements in the porous agglomerate of La<sub>0.6</sub>Ca<sub>0.4</sub>Fe<sub>0.4</sub>Mn<sub>0.6</sub>O<sub>3</sub> sample (Fig 4G) is shown in Figures 4H-L. A homogeneous bulk phase is observed with no elemental segregation. The SEM images of La<sub>0.75</sub>Sr<sub>0.25</sub>FeO<sub>3</sub>, La<sub>0.6</sub>Ca<sub>0.4</sub>MnO<sub>3</sub> and La<sub>0.6</sub>Ca<sub>0.4</sub>Fe<sub>0.4</sub>Mn<sub>0.6</sub>O<sub>3</sub> samples at their pre and post-reaction conditions are shown in Fig. S6.

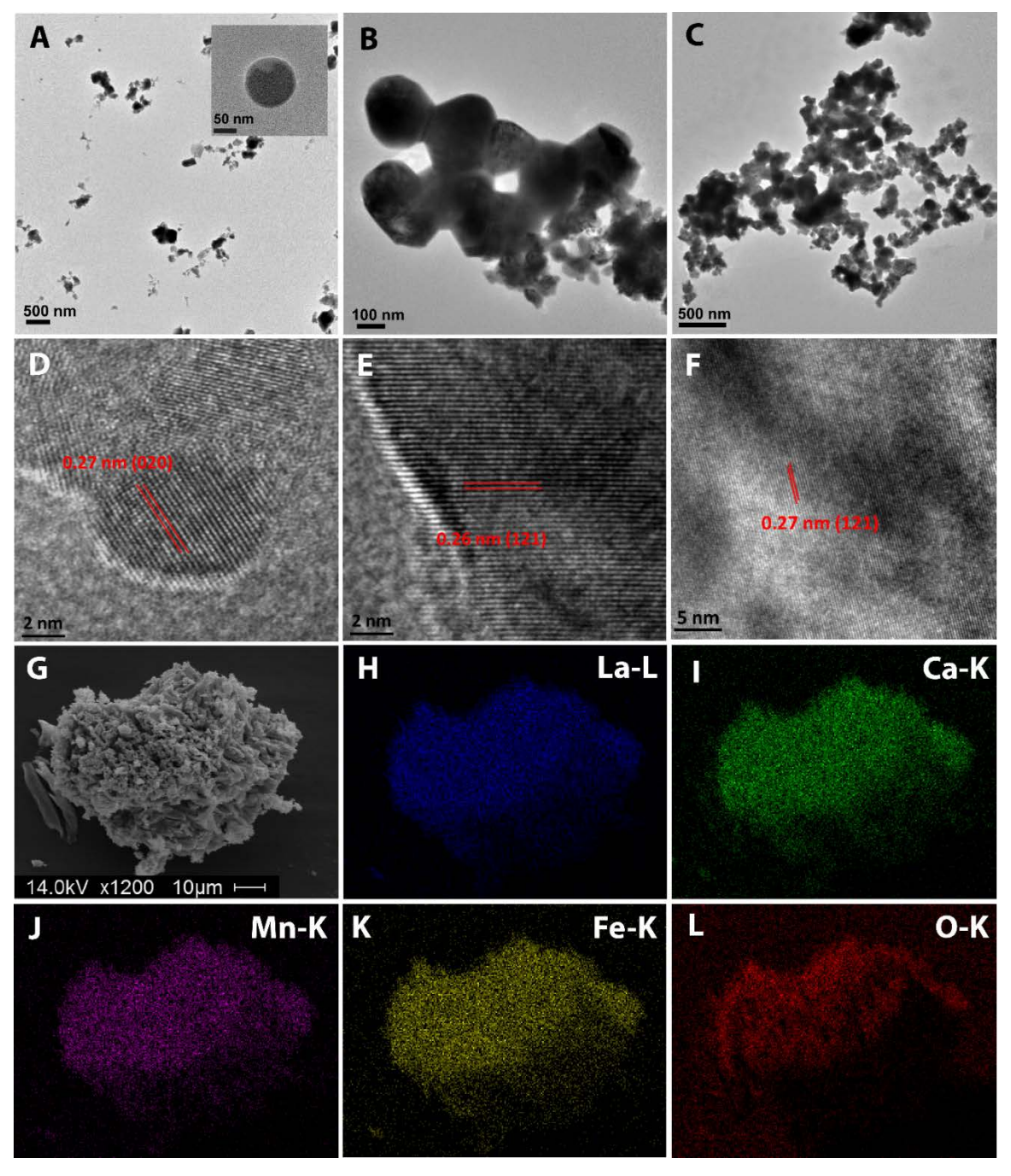


**Figure 4** | **Electron Micrographs of perovskite oxides and elemental maps via EDS. A-C,** The TEM images for La<sub>0.75</sub>Sr<sub>0.25</sub>FeO<sub>3</sub>, La<sub>0.6</sub>Ca<sub>0.4</sub>MnO<sub>3</sub>, and La<sub>0.6</sub>Ca<sub>0.4</sub>Fe<sub>0.4</sub>Mn<sub>0.6</sub>O<sub>3</sub>, while the respective HRTEM images are shown through **D-F,** SEM micrograph of La<sub>0.6</sub>Ca<sub>0.4</sub>Fe<sub>0.4</sub>Mn<sub>0.6</sub>O<sub>3</sub> is shown in **G,** while the EDS color maps for each element are shown in **H-L**.

Though, no major change in the bulk phase composition and crystallinity was observed in the samples, the XPS results of the samples revealed several surface insights. Figures 5(B-F) reveal the typical profiles of La-3d, Ca-2p, Mn-2p, Fe-2p, and O-1s orbitals of La<sub>0.6</sub>Ca<sub>0.4</sub>Fe<sub>0.4</sub>Mn<sub>0.6</sub>O<sub>3</sub>. The change in surface composition of these materials before and after the RWGS-CL cycles is

depicted in Fig. 5A. As reported in literature, we observe strontium enrichment at the surface of the LSF crystal. 57,58 This accounts for interlayer diffusion of the lanthanum and strontium near the perovskite oxide surface. However for both La<sub>0.6</sub>Ca<sub>0.4</sub>MnO<sub>3</sub> and La<sub>0.6</sub>Ca<sub>0.4</sub>Fe<sub>0.4</sub>Mn<sub>0.6</sub>O<sub>3</sub>, we observe a different trend of lanthanum enrichment at the surface. Along with these, iron becomes more predominant on the surface of La<sub>0.6</sub>Ca<sub>0.4</sub>Fe<sub>0.4</sub>Mn<sub>0.6</sub>O<sub>3</sub>. These surface enrichment of selective elements portray the role of these La-O and Fe-O based surface terminations towards increased CO<sub>2</sub> conversion performance than in LSF. The La 3d scan has a 3d<sub>5/2</sub> peak binding energy at 833.15 eV, confirming the presence of a La<sub>2</sub>O<sub>3</sub> state.<sup>59</sup> The 3d<sub>5/2</sub> multiplet splitting has a difference of ~4.4 eV, which is expected for the La<sub>2</sub>O<sub>3</sub> state. The La 3d<sub>3/2</sub> peak binding energy is at 850.02 eV. The Ca 2p scan has a  $2p_{3/2}$  peak binding energy at 345.77 eV.<sup>59</sup> The Ca  $2p_{1/2}$  has a peak at 349.35 eV.<sup>59</sup> The delta is 3.58 eV, which is an expected spin-orbit split for carbonate components. There are satellite loss features observed, which are typically present for CaCO<sub>3</sub>. These are located around ~355 and ~359 eV. The Fe 2p scan has a 2p<sub>3/2</sub> binding energy peak at 710.05 eV, corresponding top Fe (III). Fe  $2p_{1/2}$  around 723-724 eV marks the presence of both Fe (II) and Fe (III) components. 60 Fe 2p<sub>3/2</sub> satellite peaks for both Fe (II) and Fe (III) are visible around 716-719 eV range.<sup>60</sup> The Mn 2p scan has a 2p<sub>3/2</sub> peak binding energy at 641.55 eV.<sup>60,61</sup> At ~647 eV a very mild MnO satellite feature is present, which portends towards a slight presence of Mn (II) phase along with dominant Mn (III) or Mn (IV) phases. 60, 61 Two close O1s peaks are located near 531 and 529, which is expected for metal oxides. 62

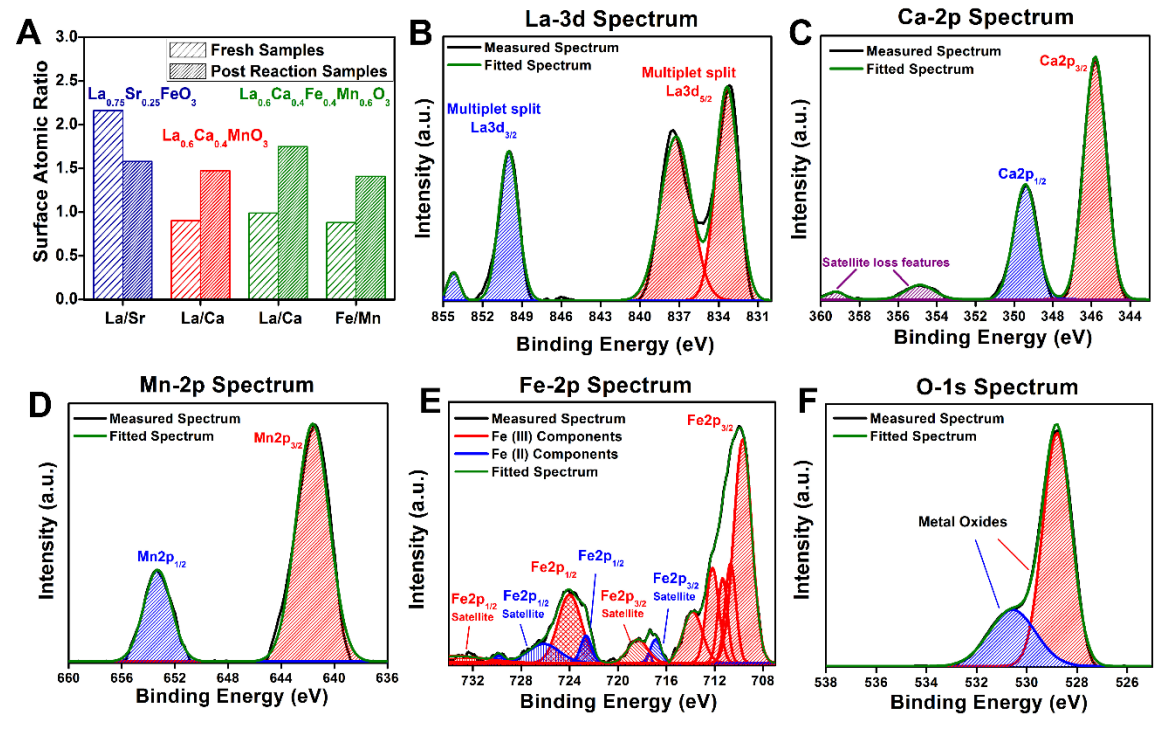


**Figure 5** | **XPS results for perovskite oxide samples. A,** Change in 'A' site and 'B' site surface elemental composition for La<sub>0.75</sub>Sr<sub>0.25</sub>FeO<sub>3</sub>, La<sub>0.6</sub>Ca<sub>0.4</sub>MnO<sub>3</sub>, and La<sub>0.6</sub>Ca<sub>0.4</sub>Fe<sub>0.4</sub>Mn<sub>0.6</sub>O<sub>3</sub> samples at pre and post reaction conditions. **B-F,** XPS profiles of the constituent elements of La<sub>0.6</sub>Ca<sub>0.4</sub>Fe<sub>0.4</sub>Mn<sub>0.6</sub>O<sub>3</sub> showing the binding energy corresponding to different orbitals.

Oxygen vacancy formation energy (E<sub>vac</sub>) essentially describes the vacancy creation step of the RWGS-CL process. For the CO<sub>2</sub> splitting step over these oxygen deficient perovskite surfaces, CO<sub>2</sub> adsorption energy (E<sub>ads</sub>) is an appropriate descriptor. CO<sub>2</sub> adsorption energies have been related to CO<sub>2</sub> conversion in RWGS-CL. <sup>15, 32</sup> For any thermochemical approach, the oxidation step of the perovskite oxide is governed by that material's oxygen affinity. This phenomenon is not limited to CO<sub>2</sub> splitting, but is applicable for water splitting as well. For all these similar processes, the surface metal on the perovskite should exhibit strong oxygen affinity so as to induce C-O or H-O bond dissociation (corresponding to CO<sub>2</sub> and H<sub>2</sub>O splitting). Since oxygen vacancy formation energy probes the energy demand of the material to create an oxygen vacancy, we believe it should exhibit similar trends to O<sub>2</sub> adsorption energy over these oxygen vacant materials. O<sub>2</sub> adsorption energy can thus be a good descriptor for oxidation step of thermochemical looping processes. Henceforth, we calculated oxygen adsorption energies (E<sub>ads</sub>) on pure stoichiometric and oxygen vacant (100) surfaces of ABO<sub>3</sub> perovskite oxides to gain insights into the reaction mechanisms. Moreover, the trends of CO<sub>2</sub> adsorption energies can be obtained through C and O adsorption energies due to scaling relations. 63-65 Since, C adsorption trend follows a similar trend as that of O adsorption, <sup>64, 65</sup> we limited our investigation to only O<sub>2</sub> adsorption energy as a model for adsorption energy of any oxygen containing gases. We studied the two dominant crystal facet terminations - 'AO' (having only 'A' site atoms and oxygen) and 'BO<sub>2</sub>' (having only 'B' site atoms and oxygen). Figs. 6(A-D) show that E<sub>ads</sub> is significantly larger on oxygen vacant surfaces irrespective of composition of the surface. Stronger O2 adsorption on these surfaces allows for easier C-O bond dissociation, proving the necessity of oxygen vacancies for better CO<sub>2</sub> reduction reaction rates. E<sub>ads</sub> trend across the 'B' site transition metals is also similar to that of Evac trend. Thus, any material reluctant to form oxygen vacancies would have strong O2 adsorption, presenting a perfect platform for dissociation of adsorbed gas molecules. On the contrary, too high an oxygen vacancy formation energy portends an energy intensive process (as shown in Fig. S4). Hence, an optimum regime of oxygen vacancy formation energy (or O<sub>2</sub> adsorption energy) exists that allows for sustainable conversion of CO<sub>2</sub>. This similarity of trends on E<sub>vac</sub> and O<sub>2</sub> adsorption energy establishes E<sub>vac</sub> as an appropriate descriptor not only for the oxygen vacancy creation step for RWGS-CL, but also for the entire RWGS-CL process as a whole. In particular, 'AO' facets are more favorable for CO<sub>2</sub> conversion than the 'BO2' facets. In particular, La-O based surface is favored for O2 adsorption, implying better CO<sub>2</sub> conversion reactions over these surfaces.<sup>32</sup> This goes to explain the reason for increased CO<sub>2</sub> conversion over La<sub>0.6</sub>Ca<sub>0.4</sub>MnO<sub>3</sub> and La<sub>0.6</sub>Ca<sub>0.4</sub>Fe<sub>0.4</sub>Mn<sub>0.6</sub>O<sub>3</sub> perovskites over LSF, as those revealed dominance of lanthanum over calcium at the crystal surface (per Fig. 5A). Hence, synthesis techniques which target AO facets are indicated for improved CO<sub>2</sub> conversion performance. These insights are not merely limited to RWGS-CL application but can be translated to other surface reactions over perovskite oxides involving oxygen evolution or oxygen reduction.

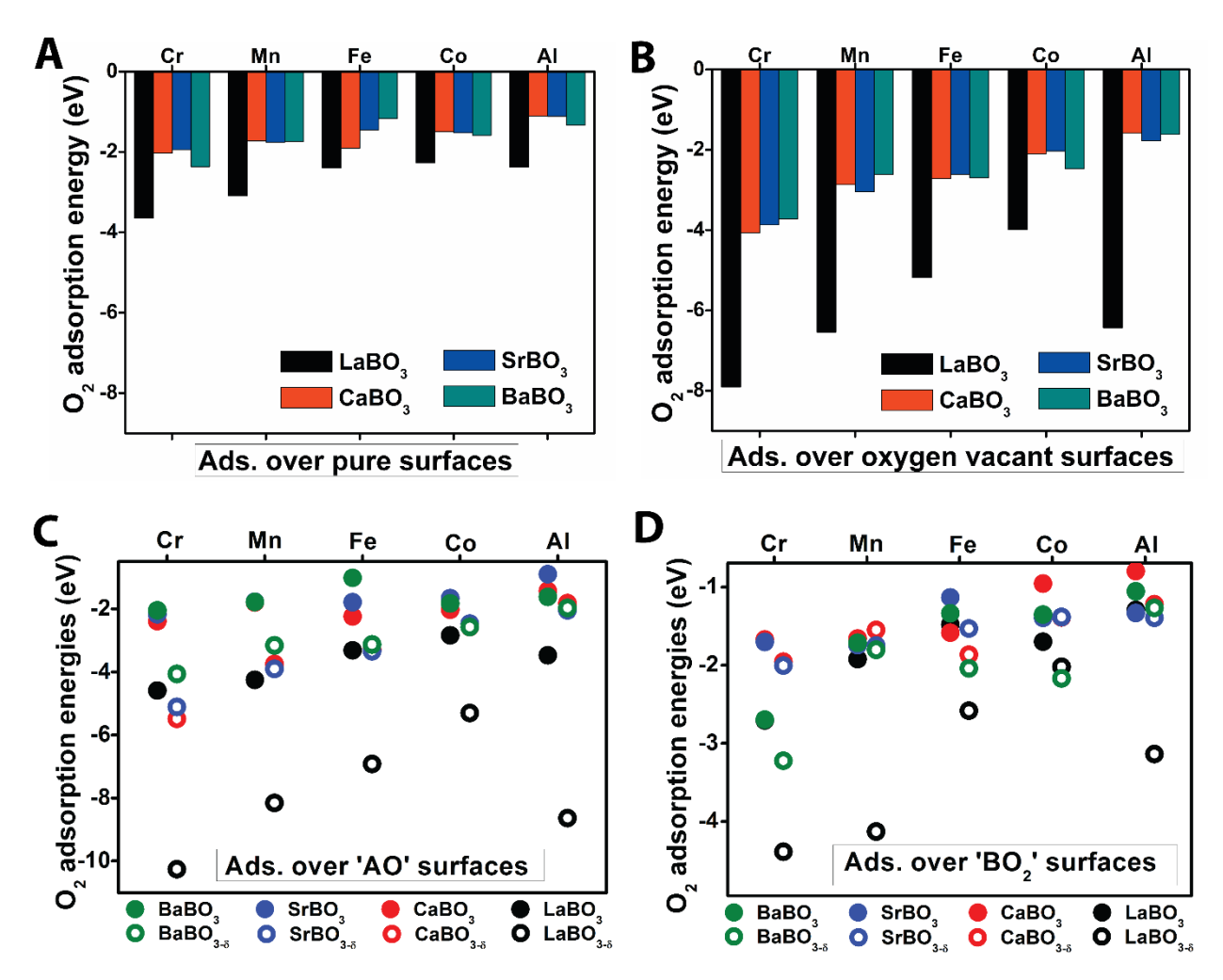


Figure 6 | O2 adsorption strengths over pure stoichiometric and oxygen vacant perovskite oxides. A, Average energy for  $O_2$  adsorption at different sites of pure 'AO' and 'BO<sub>2</sub>' terminations of (100) facets of ABO<sub>3</sub>. B, Average energy for  $O_2$  adsorption at different sites of oxygen vacant ( $\delta = 0.125$ ) 'AO' and 'BO<sub>2</sub>' terminations of (100) facets of ABO<sub>3</sub>. C, Surface specificity: average  $O_2$  adsorption energies over 'AO' sites of pure and oxygen deficient perovskites. D, Surface specificity: average  $O_2$  adsorption energies over 'BO<sub>2</sub>' sites of pure and oxygen deficient perovskites.

For any application, the intrinsic properties of a material behold the possibility of explaining that material's performance. For any catalytic reactions, material properties like oxygen vacancy formation energy ( $E_{\text{vac}}$ ), enthalpy of formation (- $H_f$ ), net electronegativity difference of the metal and the reactant, bond-dissociation energies ( $E_{\text{BDE}}$ ), band gap ( $E_g$ ), transition metal 3d band center, surface density of the transition-metals, oxidation state of the surface atoms,  $O_2$  adsorption energies,  $CO_2$  adsorption energies, other gas adsorption energies, surface enrichment of key transition metals are the usual governing parameters that can explain that material's catalytic behavior. For this particular process (RWGS-CL), oxygen vacancy creation and oxygen affinity towards refilling the vacancies are the key steps to consider. Since the decreasing trend of  $E_{\text{vac}}$  matches closely with decreasing trend of  $E_{\text{ads}}$  (as evident from Fig S4), we conclude  $E_{\text{vac}}$ 

has the potential to be the sole descriptor of this process for identifying materials with optimum E<sub>vac</sub> (which also results in desired O<sub>2</sub> adsorption properties). It is thus best said that E<sub>vac</sub> can solely describe RWGS-CL process and is capable of predicting the CO<sub>2</sub> conversion ability of perovskite oxides. Much intricate and accurate quantification of the CO<sub>2</sub> conversion performance can be provided once we delve into the surface termination effects of each material.<sup>32</sup> Investigation of these surface characteristics along with the relevant kinetic parameters (particle size, porosity, oxygen/ionic diffusivity etc.) can shed insights on the variation of CO yields of different predicted perovskite oxides as shown in Fig 3B. Recent efforts have been put forward to synthesize selective terminations over perovskite oxides. 66 These predicted new materials thus pave the way for further in-depth study of each material-set towards achieving enhanced performance for different catalytic reactions. It would be productive to unravel the dependence of DFT computed E<sub>vac</sub> of a material on its intrinsic properties. Oxygen vacancy formation in a lattice comprises of breaking of 'A-O' and 'B-O' bonds associated with the lattice oxygen being removed and the subsequent relaxation of the oxygen deficient material. Bond dissociation energies provide insights into the energy requirement for 'A-O' and 'B-O' bond cleavage, while the enthalpy of formation of a material correlates with the stability of the material. Hence, solely based on these simple parameters, an empirical model (Fig. 7A) is fitted to the DFT-computed E<sub>vac</sub> values for ABO<sub>3</sub>, A1<sub>0.5</sub>A2<sub>0.5</sub>BO<sub>3</sub>, and AB1<sub>0.5</sub>B2<sub>0.5</sub>O<sub>3</sub>. The multiple linear regression technique used for fitting a model  $E_{vac} = \beta_0 + \beta_1 H_f + \beta_1 E_{BDE}$  produced an adjusted R<sup>2</sup> value of 0.90. The model was then utilized to predict E<sub>vac</sub> of A1<sub>0.5</sub>A2<sub>0.5</sub>B1<sub>0.5</sub>B2<sub>0.5</sub>O<sub>3</sub> and was found to closely match the DFT-calculated data (Fig. 7B). The mean absolute error (MAE) between the DFT-calculated values and the model is 0.188 eV. This model is simple and can be computed from easily available E<sub>BDE</sub> values and does not require expensive band-gap based calculations. This model provides general guidelines for prediction of any other perovskite oxides for CO<sub>2</sub> conversion purposes and also for other oxygen vacancy driven applications.

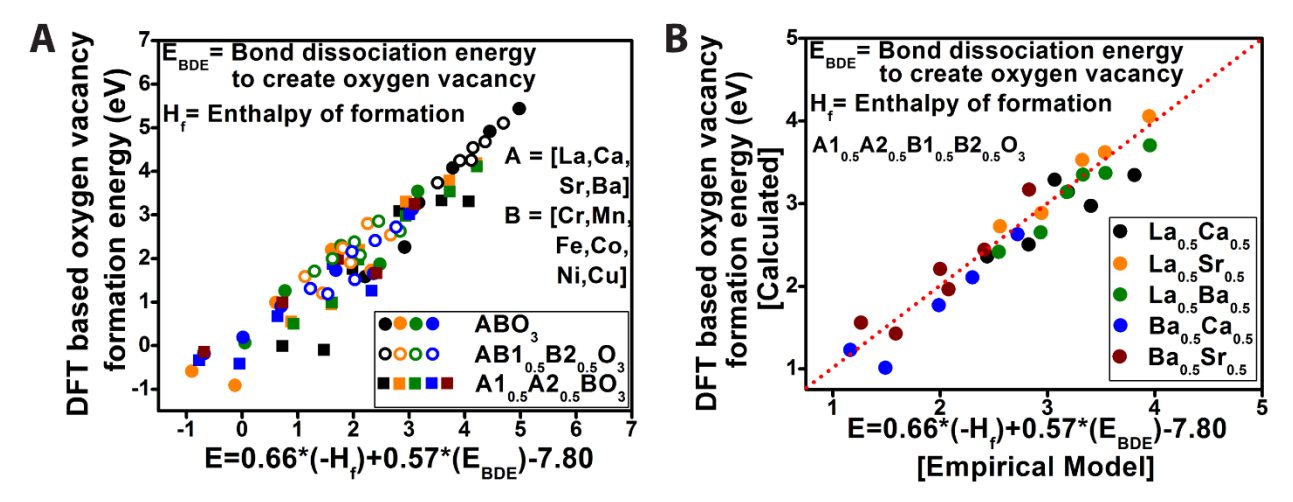


Figure 7 | Empirical modeling of oxygen vacancy formation energies ( $E_{vac}$ ) of the perovskite oxides. a, DFT-computed energies ( $E_{vac}$ ) for ABO<sub>3</sub>, A1<sub>0.5</sub>A2<sub>0.5</sub>BO<sub>3</sub>, and AB1<sub>0.5</sub>B2<sub>0.5</sub>O<sub>3</sub> were fitted to enthalpy of formation ( $H_f$ ) and bond dissociation energies ( $E_{BDE}$ ). b, The fitted model of  $E_{vac}$  was used to calculate the energies for A1<sub>0.5</sub>A2<sub>0.5</sub>B1<sub>0.5</sub>B2<sub>0.5</sub>O<sub>3</sub> system of perovskites. The DFT-calculated energy matched well with that from the empirical model.

The CO<sub>2</sub> conversion approach presented in this article enables large scale implementation in recent future, but is predicted on the cost of renewable hydrogen coming down to DOE target prices. Within that constraint, one can envision the cost of fuels produced with this technology to be in the ball park of current prices. Also, the proposed perovskites are Earth abundant and stable, which will keep operational costs low. Through this study, we have demonstrated superior CO<sub>2</sub> conversion performance via RWGS-CL at the lowest ever temperatures (~450 °C). We have shown the feasibility of these process over several new material compositions of perovskite oxides. With more detailed studies on these material sets, operational temperatures can be further lowered to ~400 °C to enable thermal integration with the subsequent FTS process. Similar STC and geothermal energy based routes are seeing implementation in small scale and pilot scale (SOLAR-JET, NewCO<sub>2</sub>Fuels Ltd., Carbon Recycling International)<sup>67-69</sup>. With better CO formation rates at lower temperatures, this process can definitely see large scale implementation in near future towards developing a closed loop carbon-neutral energy generation system. With rational DFT-calculated oxygen vacancy formation energies (E<sub>vac</sub>), we not only could propose new perovskite oxides, but also revealed the close correlation of E<sub>vac</sub> with O<sub>2</sub> adsorption, a key descriptor for many important reactions. Thus, along with improving this CO<sub>2</sub> conversion approach, this article provides avenues to improve other critical processes as well. Oxygen vacant perovskite oxides as catalytic materials have key roles in several applications such as oxygen electrocatalysis, 70-73 photocatalysis, 74 methane oxidation, 75, 76 CO and NO oxidation 77 etc. For tuning the band states and metal 3d and oxygen 2p band centers to modulate active sites for electrocatalysis, oxygen vacancy is noted to be a key parameter of interest. <sup>70,71</sup> In addition to the new perovskite oxides examined here with the oxygen vacancy formation energy model, this study will also advance frontier research on air separation technology, 78 and chemical sensing. 79

### **Conclusions:**

This study is thus an effort towards predicting and developing new materials that can convert CO<sub>2</sub> to CO at sustainable rates and temperatures that allows for thermal integration with industrially operating FTS reactors. Based on oxygen vacancy formation energy, an intrinsic material property that drives the CO<sub>2</sub> conversion reactions over perovskite oxides, we successfully predicted several earth abundant materials (A1<sub>1-x</sub>A2<sub>x</sub>B1<sub>1-y</sub>B2<sub>y</sub>O<sub>3</sub>) that demonstrated unprecedented CO<sub>2</sub> conversion performance. The empirical model developed for the oxygen vacancy formation energies can be used for future prediction of any new perovskites. It also demonstrated close correlation of oxygen vacancy formation energies to material stability (enthalpy of formation) and material composition (metal-oxygen bond dissociation energies). Oxygen adsorption energies over different stoichiometric and oxygen deficient perovskite species revealed oxygen vacant lanthanum based materials as perfect platforms for these reactions. High CO<sub>2</sub> conversion performance of lanthanum-calcium based materials at low process temperatures of 450-500 °C, calls for optimization of these material compositions that can enable future coupling of RWGS-CL with FTS for sustainable hydrocarbon generation from waste carbon dioxide.

**Acknowledgments:** The authors would like to acknowledge the financial support for this work from NSF through the awards CBET-1335817, CHE-1531590, and IIP-1743623. DM and YD thank the Office of Graduate Studies, USF for providing fellowships. YD is grateful for the McKnight Dissertation Fellowship administered by the Florida Education Fund and the Dissertation Improvement Fellowship by NASA Florida Space Grant Consortium. The authors thank the USF Research Computing for computational resources. The authors would like to thank Swetha Ramani and Dr. Yusus Emirov for their help with the microscopy. Anne J Meier at the KSC, NASA deserve special mention for her sincere help with the XPS measurements.

## **Competing financial interests:**

A provisional patent has been filed related to this work.

#### **References:**

- 1. J. Gibbins and H. Chalmers, *Energy Policy*, 2008, **36**, 4317-4322.
- 2. G. C. Institute, *The Global Status of CCS: 2016. Summary Report*, 2016.
- 3. G. J. M. Jos G. J. Olivier, Marilena Muntean, Jeroen A. H. W. Peters, *Trends in Global CO*<sub>2</sub> *emissions*, 2015.
- 4. G. Centi, E. A. Quadrelli and S. Perathoner, *Energy & Environmental Science*, 2013, **6**, 1711-1731.
- 5. G. Centi and S. Perathoner, *Catalysis Today*, 2009, **148**, 191-205.
- 6. P. Markewitz, W. Kuckshinrichs, W. Leitner, J. Linssen, P. Zapp, R. Bongartz, A. Schreiber and T. E. Muller, *Energy & Environmental Science*, 2012, **5**, 7281-7305.
- 7. D. Cheng, F. R. Negreiros, E. Aprà and A. Fortunelli, *ChemSusChem*, 2013, **6**, 944-965.
- 8. M. D. Porosoff, B. Yan and J. G. Chen, *Energy & Environmental Science*, 2016, **9**, 62-73.
- 9. K. Li, X. An, K. H. Park, M. Khraisheh and J. Tang, *Catalysis Today*, 2014, **224**, 3-12.
- 10. W. C. Chueh, C. Falter, M. Abbott, D. Scipio, P. Furler, S. M. Haile and A. Steinfeld, *Science*, 2010, **330**, 1797-1801.
- 11. P. Furler, J. R. Scheffe, M. Gorbar, L. Moes, U. Vogt and A. Steinfeld, *Energy & Fuels*, 2012, **26**, 7051-7059.
- 12. P. Furler, J. R. Scheffe and A. Steinfeld, *Energy & Environmental Science*, 2012, 5, 6098-6103.
- 13. Y. Izumi, Coordination Chemistry Reviews, 2013, 257, 171-186.
- 14. Y. A. Daza, R. A. Kent, M. M. Yung and J. N. Kuhn, *Industrial & Engineering Chemistry Research*, 2014, **53**, 5828-5837.
- 15. Y. A. Daza, D. Maiti, R. A. Kent, V. R. Bhethanabotla and J. N. Kuhn, *Catalysis Today*, 2015, **258**, **2**, 691-698.
- 16. V. V. Galvita, H. Poelman, V. Bliznuk, C. Detavernier and G. B. Marin, *Industrial & Engineering Chemistry Research*, 2013, **52**, 8416-8426.
- 17. T. Inoue, T. Iizuka and K. Tanabe, *Applied Catalysis*, 1989, **46**, 1-9.
- 18. S. Lorentzou, G. Karagiannakis, C. Pagkoura, A. Zygogianni and A. G. Konstandopoulos, *Energy Procedia*, 2014, **49**, 1999-2008.

- 19. Y. Huang, C.-F. Yan, C.-Q. Guo and S.-L. Huang, *International Journal of Photoenergy*, 2015, **2015**, 11.
- 20. E. V. Kondratenko, G. Mul, J. Baltrusaitis, G. O. Larrazabal and J. Perez-Ramirez, *Energy & Environmental Science*, 2013, **6**, 3112-3135.
- 21. J. E. Miller, M. D. Allendorf, R. B. Diver, L. R. Evans, N. P. Siegel and J. N. Stuecker, *Journal of Materials Science*, 2008, **43**, 4714-4728.
- 22. M. J. L. Ginés, A. J. Marchi and C. R. Apesteguía, *Applied Catalysis A: General*, 1997, **154**, 155-171.
- 23. D. S. Mallapragada, N. R. Singh, V. Curteanu and R. Agrawal, *Industrial & Engineering Chemistry Research*, 2013, **52**, 5136-5144.
- 24. A. H. McDaniel, E. C. Miller, D. Arifin, A. Ambrosini, E. N. Coker, R. O'Hayre, W. C. Chueh and J. Tong, *Energy & Environmental Science*, 2013, **6**, 2024-2028.
- 25. Y. A. Daza, D. Maiti, B. J. Hare, V. R. Bhethanabotla and J. N. Kuhn, *Surface Science*, 2015, **648**, 92-99.
- 26. M. Wenzel, L. Rihko-Struckmann and K. Sundmacher, *AIChE Journal*, 2016, **63**, 15-22.
- 27. M. A. Peña and J. L. G. Fierro, *Chemical Reviews*, 2001, **101**, 1981-2017.
- 28. A. T. R. Simon, Journal of Physics: Condensed Matter, 1996, 8, 8267-8275.
- 29. S. Švarcová, K. Wiik, J. Tolchard, H. J. M. Bouwmeester and T. Grande, *Solid State Ionics*, 2008, **178**, 1787-1791.
- 30. A. M. Deml, V. Stevanović, A. M. Holder, M. Sanders, R. O'Hayre and C. B. Musgrave, *Chemistry of Materials*, 2014, **26**, 6595-6602.
- 31. A. M. Deml, V. Stevanović, C. L. Muhich, C. B. Musgrave and R. O'Hayre, *Energy & Environmental Science*, 2014, 7, 1996-2004.
- 32. D. Maiti, Y. A. Daza, M. M. Yung, J. N. Kuhn and V. R. Bhethanabotla, *Journal of Materials Chemistry A*, 2016, **4**, 5137-5148.
- 33. P. Hohenberg and W. Kohn, *Physical Review*, 1964, **136**, B864-B871.
- 34. W. Kohn and L. J. Sham, *Physical Review*, 1965, **140**, A1133-A1138.
- 35. G. Kresse and J. Furthmüller, *Computational Materials Science*, 1996, **6**, 15-50.
- 36. G. Kresse and J. Furthmüller, *Physical Review B*, 1996, **54**, 11169-11186.
- 37. G. Kresse and J. Hafner, *Physical Review B*, 1993, **47**, 558-561.
- 38. G. Kresse and D. Joubert, *Physical Review B*, 1999, **59**, 1758-1775.
- 39. J. P. Perdew, K. Burke and M. Ernzerhof, *Physical Review Letters*, 1996, 77, 3865-3868.
- 40. H. J. Monkhorst and J. D. Pack, *Physical Review B*, 1976, **13**, 5188-5192.
- 41. M. T. Curnan and J. R. Kitchin, *Journal of Physical Chemistry C*, 2014, **118**, 28776–28790.
- 42. L. Wang, T. Maxisch and G. Ceder, *Physical Review B*, 2006, **73**, 195107-1 195107-6.
- 43. Y. R. Luo, *Comprehensive Handbook of Chemical Bond Energies*, Taylor & Francis, 2007.
- 44. M. Popa and M. Kakihana, *Solid State Ionics*, 2002, **151**, 251-257.
- 45. A. M. Deml, A. M. Holder, R. P. O'Hayre, C. B. Musgrave and V. Stevanović, *The Journal of Physical Chemistry Letters*, 2015, **6**, 1948-1953.
- 46. A. H. Bork, M. Kubicek, M. Struzik and J. L. M. Rupp, *Journal of Materials Chemistry A*, 2015, **3**, 15546-15557.
- 47. J. R. Scheffe, D. Weibel and A. Steinfeld, *Energy & Fuels*, 2013, **27**, 4250-4257.

- 48. L. K. Rihko-Struckmann, P. Datta, M. Wenzel, K. Sundmacher, N. V. R. A. Dharanipragada, H. Poelman, V. V. Galvita and G. B. Marin, *Energy Technology*, 2016, 4, 304-313.
- 49. M. Wenzel, N. V. R. Aditya Dharanipragada, V. V. Galvita, H. Poelman, G. B. Marin, L. Rihko-Struckmann and K. Sundmacher, *Journal of CO<sub>2</sub> Utilization*, 2017, **17**, 60-68.
- 50. N. G. A. Earnshaw, *Chemistry of the Elements*, Elsevier, 1997.
- 51. P. Kaiser, R. B. Unde, C. Kern and A. Jess, *Chemie Ingenieur Technik*, 2013, **85**, 489-499.
- 52. W. Wang, S. Wang, X. Ma and J. Gong, Chemical Society Reviews, 2011, 40, 3703-3727.
- 53. T. Riedel, G. Schaub, K.-W. Jun and K.-W. Lee, *Industrial & Engineering Chemistry Research*, 2001, **40**, 1355-1363.
- 54. A. Lebouvier, S. A. Iwarere, P. d'Argenlieu, D. Ramjugernath and L. Fulcheri, *Energy & Fuels*, 2013, **27**, 2712-2722.
- 55. T. Abe, M. Tanizawa, K. Watanabe and A. Taguchi, *Energy & Environmental Science*, 2009, **2**, 315-321.
- 56. C. Graves, S. D. Ebbesen, M. Mogensen and K. S. Lackner, *Renewable and Sustainable Energy Reviews*, 2011, **15**, 1-23.
- 57. J. Druce, H. Tellez, M. Burriel, M. D. Sharp, L. J. Fawcett, S. N. Cook, D. S. McPhail, T. Ishihara, H. H. Brongersma and J. A. Kilner, *Energy & Environmental Science*, 2014, 7, 3593-3599.
- 58. J. N. Kuhn and U. S. Ozkan, *Journal of Catalysis*, 2008, **253**, 200-211.
- 59. Thermo Scientific Avantage Data System for XPS, (https://xpssimplified.com/periodictable.php).
- 60. M. C. Biesinger, B. P. Payne, A. P. Grosvenor, L. W. M. Lau, A. R. Gerson and R. S. C. Smart, *Applied Surface Science*, 2011, **257**, 2717-2730.
- 61. I. Uhlig, R. Szargan, H. W. Nesbitt and K. Laajalehto, *Applied Surface Science*, 2001, **179**, 222-229.
- 62. H. Nohira, W. Tsai, W. Besling, E. Young, J. Petry, T. Conard, W. Vandervorst, S. De Gendt, M. Heyns, J. Maes and M. Tuominen, *Journal of Non-Crystalline Solids*, 2002, **303**, 83-87.
- 63. E. M. Fernández, P. G. Moses, A. Toftelund, H. A. Hansen, J. I. Martínez, F. Abild-Pedersen, J. Kleis, B. Hinnemann, J. Rossmeisl, T. Bligaard and J. K. Nørskov, *Angewandte Chemie International Edition*, 2008, 47, 4683-4686.
- 64. R. Michalsky, Y.-J. Zhang, A. J. Medford and A. A. Peterson, *The Journal of Physical Chemistry C*, 2014, **118**, 13026-13034.
- 65. F. Calle-Vallejo, J. I. Martínez, J. M. García-Lastra, J. Rossmeisl and M. T. M. Koper, *Physical Review Letters*, 2012, **108**, 116103.
- 66. X. Ma, J. S. A. Carneiro, X.-K. Gu, H. Qin, H. Xin, K. Sun and E. Nikolla, *ACS Catalysis*, 2015, **5**, 4013-4019.
- 67. SOLAR-JET, <a href="http://www.solar-jet.aero/">http://www.solar-jet.aero/</a>, (accessed 11.26.2017, 2017).
- 68. New CO2 Fuels, http://www.newco2fuels.co.il/, (accessed 11.26.2017, 2017).
- 69. Carbon Recycling International (CRI), <a href="http://carbonrecycling.is/">http://carbonrecycling.is/</a>, (accessed 11.26.2017, 2017).
- 70. J. Suntivich, K. J. May, H. A. Gasteiger, J. B. Goodenough and Y. Shao-Horn, *Science*, 2011, **334**, 1383.

- 71. J. Suntivich, H. A. Gasteiger, N. Yabuuchi, H. Nakanishi, J. B. Goodenough and Y. Shao-Horn, *Nat Chem*, 2011, **3**, 546-550.
- 72. K. Zhu, T. Wu, M. Li, R. Lu, X. Zhu and W. Yang, *Journal of Materials Chemistry A*, 2017, **5**, 19836-19845.
- 73. J. T. Mefford, X. Rong, A. M. Abakumov, W. G. Hardin, S. Dai, A. M. Kolpak, K. P. Johnston and K. J. Stevenson, *Nature Communications*, 2016, 7, 11053.
- 74. H. Tan, Z. Zhao, W.-b. Zhu, E. N. Coker, B. Li, M. Zheng, W. Yu, H. Fan and Z. Sun, *ACS Applied Materials & Interfaces*, 2014, **6**, 19184-19190.
- 75. K. Nomura, T. Hayakawa, K. Takehira and Y. Ujihira, *Applied Catalysis A: General*, 1993, **101**, 63-72.
- 76. M. D. Krcha, A. D. Mayernick and M. J. Janik, Journal of Catalysis, 2012, 293, 103-115.
- 77. V. Torregrosa-Rivero, V. Albaladejo-Fuentes, M.-S. Sanchez-Adsuar and M.-J. Illan-Gomez, *RSC Advances*, 2017, **7**, 35228-35238.
- 78. H.-C. Wu and Y. S. Lin, *Industrial & Engineering Chemistry Research*, 2017, **56**, 6057-6064.
- 79. A. Kolmakov and M. Moskovits, *Annual Review of Materials Research*, 2004, **34**, 151-180.